ENVIRONMENTAL RESEARCH
COMMUNICATIONS

ACCEPTED MANUSCRIPT • OPEN ACCESS

Responses of Summer Mesoscale Convective Systems to Irrigation over the North China Plain based on Convection-Permitting Model Simulations

To cite this article before publication: Yixiao Wang *et al* 2024 *Environ. Res. Commun.* in press https://doi.org/10.1088/2515-7620/ad78ba

Responses of Summer Mesoscale Convective Systems to Irrigation over the North China Plain based on Convection-Permitting Model Simulations

Yixiao Wang[1], Ben Yang[1,2,3], Zhao Yang[4], Zhe Feng[4], Bo Qiu[1], Guoqing Dai[1], Yun Qian[4], Yaocun Zhang[1,2]

[1] School of Atmospheric Sciences, Nanjing University, Nanjing, Jiangsu, China

[2] China Meteorological Administration Key Laboratory for Climate Prediction Studies, Nanjing University, Nanjing, China

[3] Frontiers Science Center for Critical Earth Material Cycling, Nanjing University, Nanjing, Jiangsu, China

[4] Pacific Northwest National Laboratory, Richland, Washington, USA

Correspondence to Ben Yang byang@nju.edu.cn

To be revised to *Environmental Research Communications*

August 2024

Abstract

Extensive irrigation activities in the North China Plain (NCP) significantly influence regional weather and climate. However, previous studies focusing on the NCP were primarily based on coarse-resolution models, which are unable to explicitly resolve convection systems, causing large uncertainty in precipitation simulations. In this study, a convection-permitting model coupled with a dynamic irrigation scheme is utilized to investigate the impacts of irrigation on summertime mesoscale convective systems (MCSs) over the NCP. Sensitivity experiments with irrigation off and on are conducted for 5 summers and an MCS identification and tracking algorithm is applied to both satellite observations and model simulations. We find that incorporating irrigation in the model increases MCS precipitation, which agrees more with observations. The probability distributions of MCS lifetime, area, propagation speed, and intensity are all better simulated with irrigation. Irrigation increases the occurrence frequency of MCSs throughout the entire day. The nighttime increase is partly because of more frequent local initiation of MCS developed from isolated deep convection, while the daytime increase is mainly attributed to the changes in MCSs initiating elsewhere and then propagating to the NCP. On average, irrigation induces additional moisture that is more thermodynamically favorable for precipitation, but this effect is partially offset by the weakened ascending air motion primarily caused by irrigation surface cooling. Compared to weak MCS precipitation events, strong MCS precipitation events experience greater enhancement in precipitation intensity when including irrigation because the offset effect from the change in large-scale ascending air motion is insignificant. In addition, irrigation makes the variation of MCS precipitation intensity more correlated with the variation in ascending motion but less correlated with that in atmospheric moisture. Our results suggest the pronounced impacts of irrigation on MCSs over the NCP which should be included in numerical models to improve regional precipitation simulation and prediction.

Keywords: irrigation, mesoscale convective systems, North China Plain, convection-permitting model

1 Introduction

Irrigation, which consumes approximately 70% of total freshwater withdrawals in the globe (Siebert *et al* 2010), plays a crucial role in ensuring food security, managing water resources, and fostering economic development. By adding extra water to the soil, irrigation increases latent heat flux and decreases sensible heat flux, which generally lead to a reduction in daytime near-surface temperature (e.g., Adegoke *et al* 2003, Mahmood *et al* 2006, Sacks *et al* 2009, Yang *et al* 2016, Yang *et al* 2017).

The relationship between irrigation and precipitation is intricate, as it is influenced by complex feedbacks between land and atmosphere. Two competing land-atmosphere feedback mechanisms have been identified in the local impacts of irrigation on precipitation. Both observational and numerical modeling studies have suggested that, the cooling effect of irrigation lowers the planetary boundary layer and increases convective inhibition (Crook 1996, DeAngelis *et al* 2010, Douglas *et al* 2009). Meanwhile, as irrigation enhances local evaporation, the moistening of the low-level atmosphere contributes to an increase in convective available potential energy, favoring more convective precipitation (Crook 1996, Pielke 2001, Yang *et al* 2017). Additionally, irrigation can induce remote impacts on precipitation. For instance, the excessive downstream precipitation can be attributed to the moisture and energy gradients between irrigated and downwind areas, which lead to moisture convergence in the downwind region (Alter *et al* 2015, Pei *et al* 2016). Irrigation also triggers secondary atmospheric circulation, which in turn affects regional precipitation and streamflow (Kanamitsu and Mo 2003; Yang *et al* 2017).

Deep convection is a primary cause of meteorological hazards such as tornadoes, flash floods, hail, and thunderstorms (Houze 2004, Hu *et al* 2020, Schumacher and Rasmussen 2020, Smith *et al* 2012, Stevenson and Schumacher 2014), posing a considerable threat to human life and property. The impact of deep convection intensifies when they evolve into mesoscale dimensions, characterized by organized storms distinct from isolated convective storms. Mesoscale convective systems (MCSs) are the most prominent manifestation of deep convection, which is long-lived and can cover a precipitation area with a length scale larger than 100 km (Houze 2004, 2018, Markowski and Richardson 2010). MCSs manifest across diverse regions, including the tropics (Feng *et al* 2021, Huang *et al* 2018, Nesbitt *et al* 2006, Yuan and Houze 2010), East Asia (Fu *et al* 2019, Kukulies *et al* 2021, Li *et al* 2020, Yang *et al* 2015, Yang *et al* 2019, Zhang *et al* 2018, Zhang *et al* 2019), the United States (Feng *et al* 2019, Haberlie and Ashley 2019, Laing and Fritsch 1997, Schumacher and Rasmussen 2020), and South America (Anabor *et al* 2008, Rasmussen *et al* 2016, Salio *et al* 2007) contributing to more than half of the precipitation in these areas (Feng *et al* 2021).

With the advancement of computational capabilities, convection-permitting models (CPMs) with horizontal grid spacing of several kilometers have become increasingly prevalent in regional climate simulations (Gutowski *et al* 2020). These models have been proven effective in mitigating modeling uncertainty associated with parameterizations of deep convection (Ban *et al* 2014, Fosser *et al* 2015, Kendon *et al* 2012). Additionally, their finer spatial resolutions offer a more comprehensive depiction of surface heterogeneities (Lucas-Picher *et al* 2021). By explicitly resolving deep convection, CPMs can better simulate various precipitation characteristics such as the diurnal cycle, frequency, intensity, spatial and temporal distributions, and extreme events. CPMs have been widely applied in simulating MCSs (Feng *et al* 2018, Feng *et* *al* 2023b, Prein *et al* 2020, Yang *et al* 2023, Yun *et al* 2021). Recent CPM studies showed that irrigation enhances summer MCS precipitation in the irrigated area (Qian *et al* 2020) and its downstream regions (Li *et al* 2022) in the United States.

The North China Plain (NCP, 34°–41°N; 113°–121°E; figure 1), which occupies an area of about 400,000 km^2, is one of the most densely populated regions in the world (Kang and Eltahir 2018, 2019). Meanwhile, the NCP is the largest irrigated region (Kang and Eltahir 2019) and the primary crop-producing area in China. The double cropping system of winter wheat and summer maize in the NCP accounts for 75% and 35% of China's wheat and maize production, respectively (Mo *et al* 2017). The water consumption rate of summer maize is 3.39 mm day^{-1} (Kong *et al* 2012), with an irrigation water requirement of 250.5 mm in the NCP (Wu *et al* 2019) and an irrigation area fraction exceeding 40% in the region (figure 1(b)). In summer, the MCS events are active in the NCP, especially in July and August (Li *et al* 2020), significantly impacting agricultural productivity and the regional economy. The extensive and continually expanding irrigation activities in the NCP significantly influence surface humidity and temperature, the surface energy budget, and the development of the boundary layer (Yang *et al* 2016). Previous studies have also demonstrated that irrigation has notable impacts on precipitation over the NCP (Zhang *et al* 2015, Yang *et al* 2016, Kang and Eltahir 2018, 2019, Liu *et al* 2021, Fan *et al* 2023). However, these studies were predominantly based on observations or coarse-resolution model simulations that do not explicitly resolve convective processes. In this study, we used the Weather Research and Forecasting Model (WRF) coupled with a dynamic irrigation scheme to conduct convection-permitting simulations at 4 km horizontal grid spacing with a dynamic irrigation over the NCP. An objective MCS identification and tracking algorithm is applied. Our main objectives are to investigate the impacts of irrigation on summertime MCSs over the NCP and to examine how the inclusion of irrigation helps improve simulations of MCSs and their associated precipitation. The physical mechanisms associated with the response of MCSs are also analyzed.

2 Data and Methods

2.1 WRF Model Setup

The WRF model version 4.3.3 (Skamarock *et al* 2019) is used in this study. Two nested domains with horizontal grid spacings of 12 km and 4 km are configured (figure 1(a)), and the outer domain simulations are used to drive the inner domain via lateral boundaries by applying the one-way nesting approach through the ndown program. The outer domain encompasses 5°–53°N and 82°–146°E, while the inner domain encompasses 20°–43°N and 98°–130°E. There are 40 vertical layers from the surface to 50 hPa. Model outputs are saved at 1 h intervals.

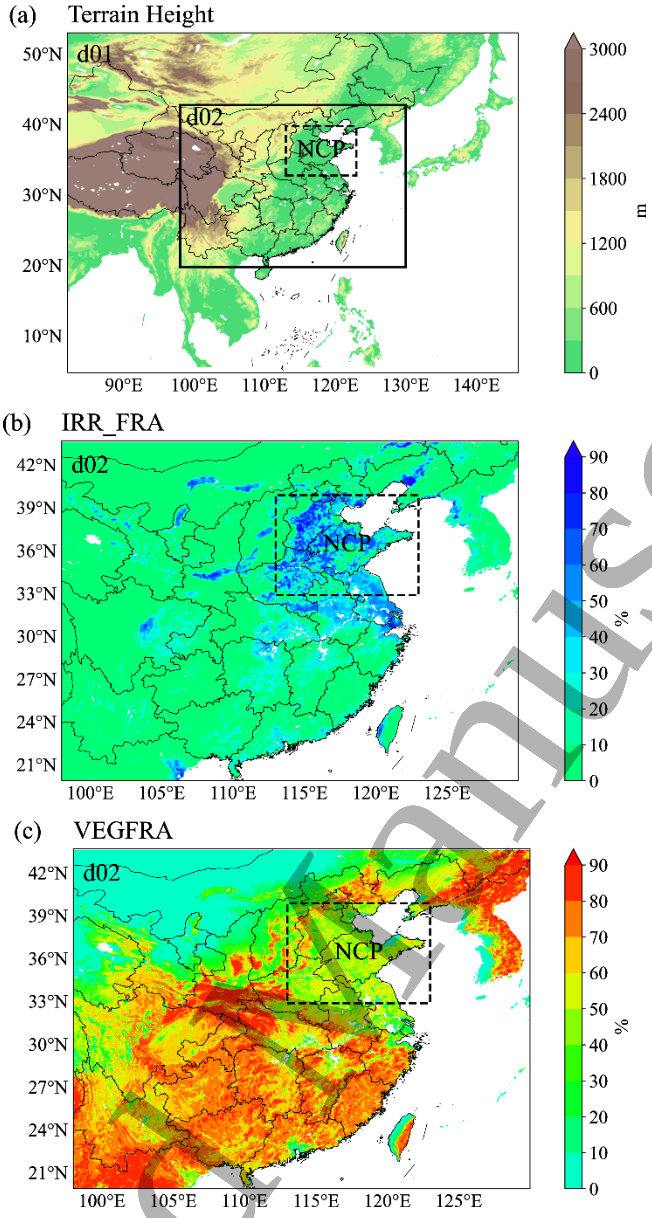

Figure 1. (a) Topography (shaded; units: m) within the two nested domains. (b) Irrigation fraction and (c) averaged fractional vegetation coverage during the simulated period in the inner domain. The dashed boxes denote the main research region in this study (113°–123°E, 33°–40°N).

The physical parameterizations used in the model are listed in table 1. To simulate the effects of irrigation, we implement an irrigation scheme (Ozdogan *et al* 2010) into the Noah Land Surface Model in WRF (figure 1(b)) following Qian *et al* (2013) and Yang *et al* (2016). The irrigation scheme determines where to irrigate based on the land use types from MODIS and the irrigation fraction derived from the Food and Agriculture Organization of the United Nations (Siebert *et al* 2013). In this study, irrigation is activated in grid cells classified as grassland or cropland where the irrigation fraction exceeds 0. Additionally, when and how to irrigate are primarily controlled by vegetation and soil characteristics, including Green Vegetation Fractions (GVFs), root-zone soil moisture content and soil water field capacity. More details about the irrigation scheme can be found in Ozdogan *et al* (2010), Qian *et al* (2013) and Yang *et al* (2016).

Table 1. Physical parameterizations used in the model simulations.

Physical Process	Parameterization Scheme
Cumulus Physics (Outside Model Domain)	Tiedtke Scheme (Tiedtke 1989, Zhang *et al* 2011)
Microphysics	Thompson Scheme (Thompson *et al* 2008)
Radiation	RRTMG Shortwave and Longwave Schemes (Iacono *et al* 2008)
Planetary Boundary Layer Physics	MYNN2 scheme (Nakanishi and Niino 2006)
Surface Layer	Eta Similarity Scheme (Janjic 1996, 2001)
Land Surface	Unified Noah Land Surface Model (LSM; Tewari 2004)

The initial and boundary conditions for the outer domain are derived from the National Centers for Environmental Prediction (NCEP) operational global final (FNL) analyses data (1° × 1°) with an interval of 6 h (NCEP, 2000), which is downscaled to 12 km to provide cost-effective and relatively reliable lateral boundary conditions for the 4 km inner domain (Kadaverugu *et al* 2021; Klausmann *et al* 2014). The FNL data is also employed to update sea surface temperatures in all the WRF model simulations and to apply analysis nudging for horizontal wind, temperature, and water vapor mixing ratio in the outer domain, providing more accurate lateral boundary conditions (LBCs) for the inner domain. The moderate resolution imaging spectroradiometer (MODIS) 21-category land type data with a resolution of 1 km in 2005 is used to obtain the model land cover information. To represent the comprehensive seasonal variation of plants, the default GVFs in the model are replaced by the average of 2008–2018 Fractional Vegetation Coverage (FVC) from the Global Land Surface Satellite (GLASS) product with 0.25° × 0.25° grid spacing and 8-day intervals (Liang *et al* 2021) (figure 1(c)).

To quantify the impacts of irrigation on the summertime MCS, two simulations with irrigation off (i.e., CNTL) and on (i.e., IRR) are performed from May 20 to August 31 over a 5-year period (2015–2019), with a spin-up time from May 20 to May 31.

2.2 The FLEXTRKR Algorithm for MCS Identification and Tracking

In this study, deep convective systems, including isolated deep convection (IDCs) and MCSs, are identified and tracked using the FLEXible object TRacKeR (FLEXTRKR) algorithm (Feng *et al* 2023a) in both observations and model simulations based on brightness temperature (T_b) and precipitation fields. A cold cloud system (CCS) is first identified as cold cloud cores (T_b < 225 K) that iteratively expand to reach 241 K. CCSs are then tracked if areas of two CCSs between consecutive time steps overlap by more than 50%. Based on precipitation feature (PF, contiguous area with rain rate > 2 mm hr^{-1}) characteristics, MCSs are defined as large and long-lived CCSs that encompass an area > 40,000 km^2, containing a PF with a major axis length > 100 km for longer than 4 continuous hours. The PF area, mean rain rate, rain rate skewness, and heavy rain volume ratio must exceed the corresponding lifetime-dependent thresholds provided by Feng *et al* (2021). Furthermore, IDCs are defined as relatively small CCSs that are identified as convective updraft and convection by the SL3D algorithm (Starzec *et al* 2017) but do not meet the criteria of MCSs.

To eliminate the effect of resolution disparities between simulations and observations, the precipitation and brightness temperature data from the 4 km simulations are re-gridded using bilinear interpolation to match the 10 km grid spacing of the observational data (see section 2.3.1) before identifying MCSs. In addition, to analyze the impacts of irrigation on IDCs, a different set of tracking runs is conducted based on the native 4-km model outputs because the 10-km grid spacing is too coarse to identify IDCs.

2.3 Data for Model Evaluation

2.3.1 Satellite Data for MCS Tracking

To evaluate the simulated MCSs in both CNTL and IRR, the NASA Global Merged IR V1 infrared brightness temperature (T_b) data (Janowiak *et al* 2017) and the Global Precipitation Measurement (GPM) Integrated Multi-satellitE Retrievals (IMERG) V06 B precipitation data (Huffman *et al* 2019) are used for observational MCSs identification. The global T_b data set is a merged geostationary satellite data set, covering from 60°S to 60°N globally with a horizontal resolution of about 4 km and a temporal resolution of 30 min. The 0.1° × 0.1° and 30-min GPM IMERG data set is a unified precipitation retrieval based on passive microwave sensors and infrared geostationary satellite rainfall retrievals. Following Feng *et al* (2021), the global T_b data set is re-gridded to match the grid spacing of the GPM IMERG data set. To align with the time interval of model simulations, the 30-min IMERG precipitation data is averaged to hourly intervals, and the hourly T_b data at 00 min is used to represent convective clouds for that hour. The combined T_b and precipitation data for observational MCS identification covers the same region and time period as model simulations, with a ~10-km and 1-h resolution.

2.3.2 Surface Observational Data for Model Evaluation

The model results of 2 m air temperature and 2 m relative humidity are evaluated using the 0.25° × 0.25° CN05.1 dataset (Wu and Gao 2013, Wu *et al* 2017), which is constructed by interpolating data from 2,400 observation stations across China. The hourly averaged GPM IMERG precipitation dataset is used to verify the model simulated precipitation.

3 Results

3.1 Simulated Versus Observed Near-surface Properties and Precipitation

We first evaluate the simulated temperature and relative humidity (RH) at 2 m height and surface precipitation against observations (figure 2). The CNTL experiment reveals a significant warm bias of approximately 0.5–3.5 °C in northwest China and the NCP (figure 2(a)). There are also significant underestimations of RH over the NCP and its adjacent regions (figure 2(b)), with the average dry bias exceeding 4.5% and maximum bias reaching 13.5% in the central NCP. Additionally, the CNTL experiment exhibits a notable underestimation of precipitation by 0.3–2.1 mm day^{-1} across nearly the entire NCP (figure 2(c)) except in areas with complex terrain (figure 1(a)).

When incorporating irrigation into the model, the warm biases in the 2 m temperature are reduced to 0–1.5 °C (figure 2(d)) and the dry biases in RH are reduced to 1.5–13.5% (figure 2(e)) over the irrigated areas. In the NCP, the mean bias and root mean square error (RMSE) of the 2 m temperature are 0.7 °C and 2.3 °C in the IRR experiment, respectively, which are lower than the values in the CNTL experiment (i.e., 1.2 °C and 2.6 °C). Meanwhile, the mean bias and RMSE of RH is -4.8% and 11.1% in IRR, compared to -9.4% and 14.2% in CNTL. The impact of irrigation on total precipitation amount is relatively small (figure 2(f)). With irrigation included, the underestimation of precipitation is slightly mitigated from -0.65 mm day^{-1} to -0.49 mm day^{-1} averaged in the NCP.

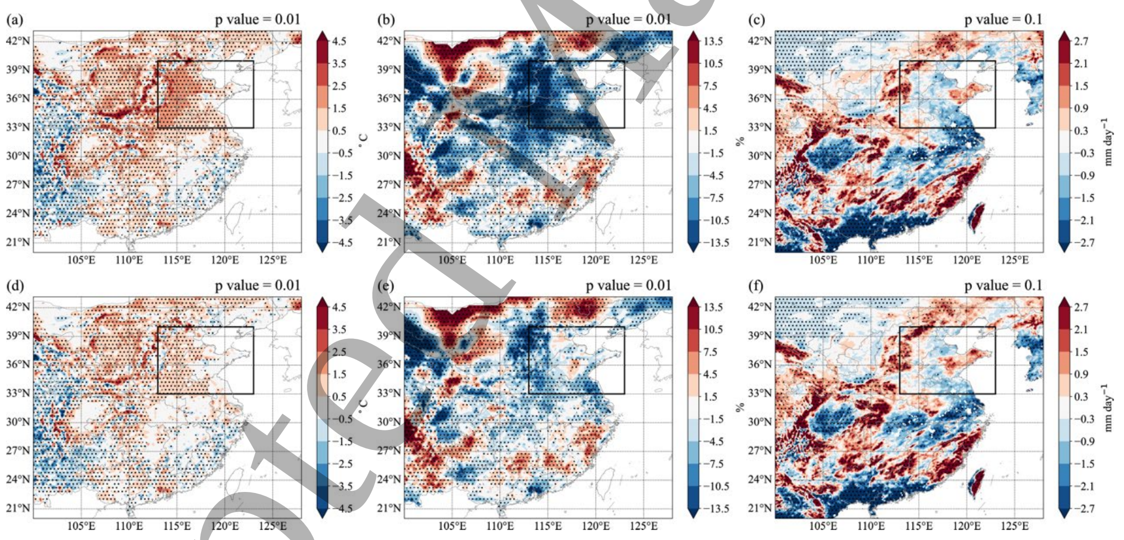

Figure 2. Spatial distributions of differences in (a and d) 2 m temperature (shaded; units: °C), (b and e) 2 m relative humidity (shaded; units: %), and (c and f) precipitation (shaded; units: mm day^{-1}) during the five summers of 2015-2019. The upper and lower rows represent CNTL minus Observations and IRR minus Observations, respectively. The dotted areas denote where the differences are statistically significant (t-test) at confidence levels of 99%, 99%, and 90% for 2 m temperature, 2 m relative humidity, and precipitation, respectively. The solid boxes denote the NCP.

The latitude–time variations of summer precipitation are depicted in figure 3. In the observation, the monsoon rain belt begins to approach the southern part of the NCP on June 20 (figure 3(a)). It then advances to the central and northern NCP on July 10, remaining in the NCP for about one month. Both the CNTL and IRR simulations can generally capture the seasonal progression of the monsoon precipitation well (figures 3(b) and (c)).

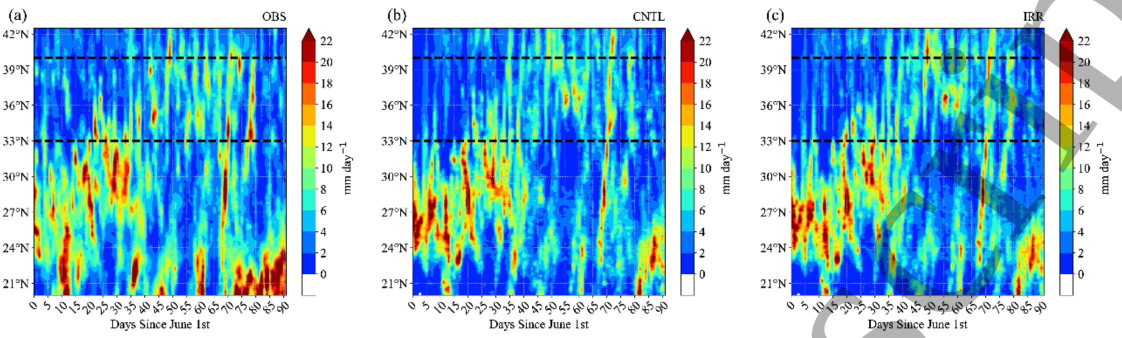

Figure 3. Latitude–time diagram of precipitation (shaded; units: mm day^{-1}) averaged at 113°–123°E of (a) Observations, (b) CNTL and (c) IRR, respectively. The dashed black lines denote the latitudinal range of the NCP.

3.2 Irrigation Effects on MCSs

Because the spatial resolution of 10 km is too coarse to identify IDCs, we utilize the FLEXTRKR algorithm to classify precipitation into MCS and non-MCS types when comparing the simulations with observations (see section 2.2). Observational data indicates that more than 70% of the total summer precipitation in the northwestern part of the domain is contributed by non-MCS types (figure 4(a)). The contribution of MCSs gradually increases from northwest to southeast (figure 4(b)). In the NCP, MCSs contribute to 30%–60% of the total precipitation (figure 4(b)). Notably, CNTL underestimates the MCS contribution while overestimating the non-MCS contribution (figures 4(c) and (d)). Compared to CNTL, the MCS contributions in IRR are 6%–18% higher over the irrigated areas in the NCP (figures 4(h)), agreeing more with observations (figures 4(f)).

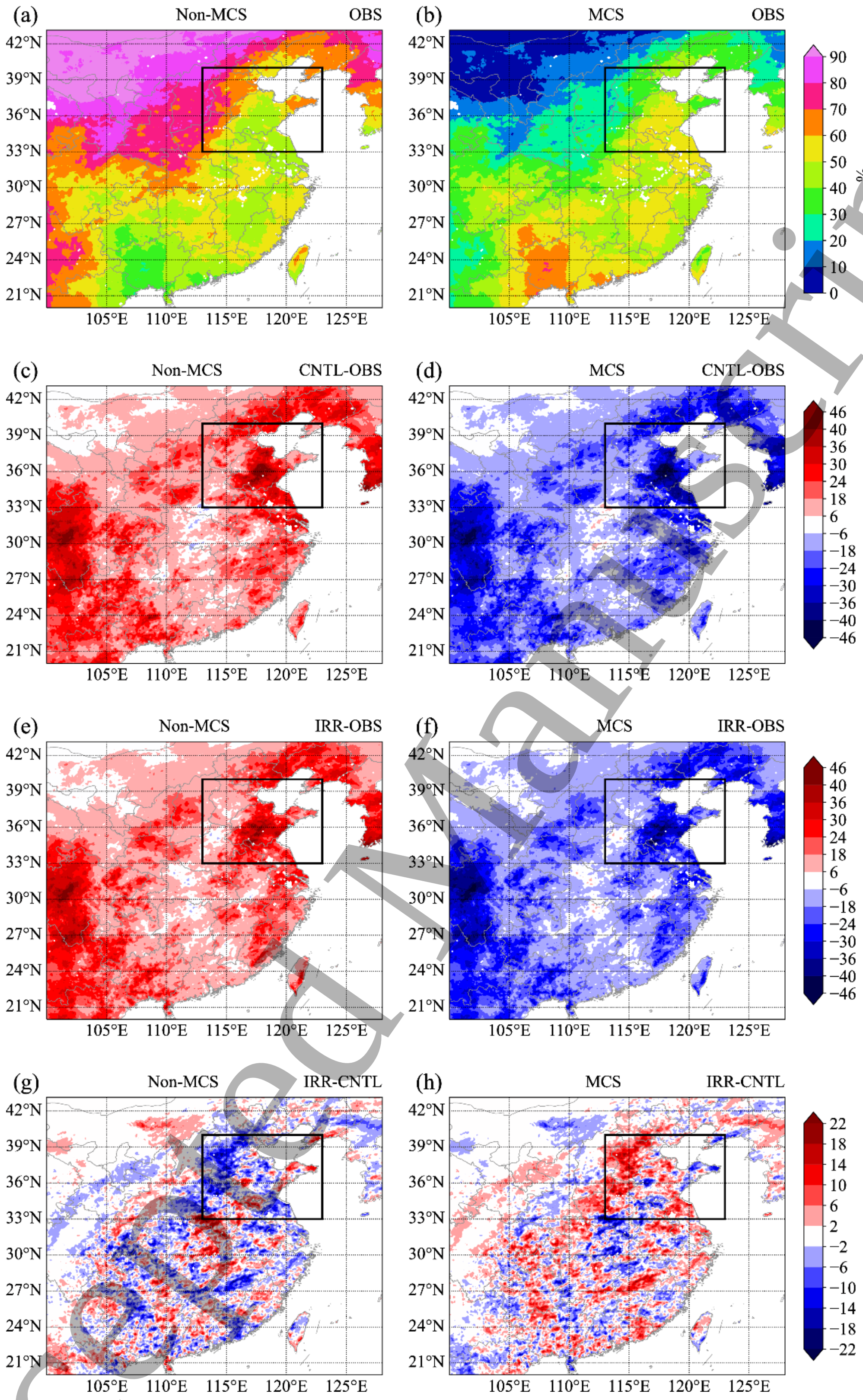

Figure 4. Spatial distributions of contributions of Non-MCS (left column) and MCS (right column) to summer precipitation in (a and b) observations (shaded; units: %), (c and d) CNTL minus observations (shaded; units: %), (e and f) IRR minus observations (shaded; units: %), and (g and h) IRR minus CNTL (shaded; units: %). The solid boxes denote the NCP.

Aligning with the re-gridded 10-km results (figure 4(h)), the tracked MCSs based on the native 4-km model outputs (figure 5) also reveal that the MCSs' contributions to total precipitation are increased by 6%–18% due to irrigation in the NCP (figure 5(a)). Correspondingly, the contributions of IDCs in the NCP are reduced (figure 5(b)).

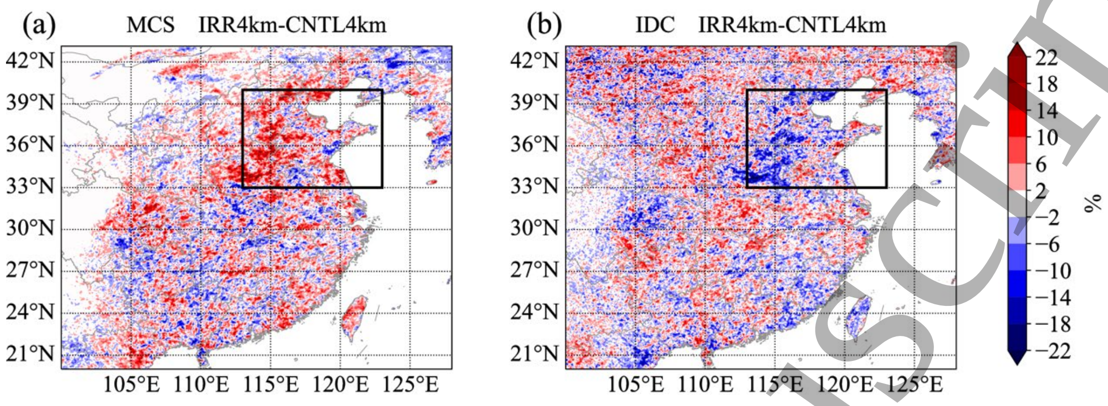

Figure 5. Spatial distributions of contributions of (a) MCSs (shaded; units: %) and (b) IDCs (shaded; units: %) to summer precipitation in IRR minus CNTL based on the original 4-km model outputs. The solid boxes denote the NCP.

The diurnal cycles of MCS and IDC occurrence frequencies are shown in figures 6(a) and (b), suggesting that MCSs and IDCs are mostly nighttime and daytime events, respectively. Compared to the nighttime peak of MCS frequency, MCSs mostly initiate during the day (figure 6(c)) and persist through the night (figure 6(d)). Irrigation increases the frequency of MCSs both during the day and at night while decreasing nighttime IDCs (red lines). Meanwhile, irrigation leads to more initiation of MCSs at night (figures 6(c) and (d)), corresponding well to the decreases of nighttime IDCs, indicating that more local IDCs are able to develop into organized and long-lived systems at night in the NCP. By comparing figures 6(a) and (d), we can infer that the increase in daytime MCSs is mainly contributed by the changes in MCSs which initiate far away and then propagate to the NCP.

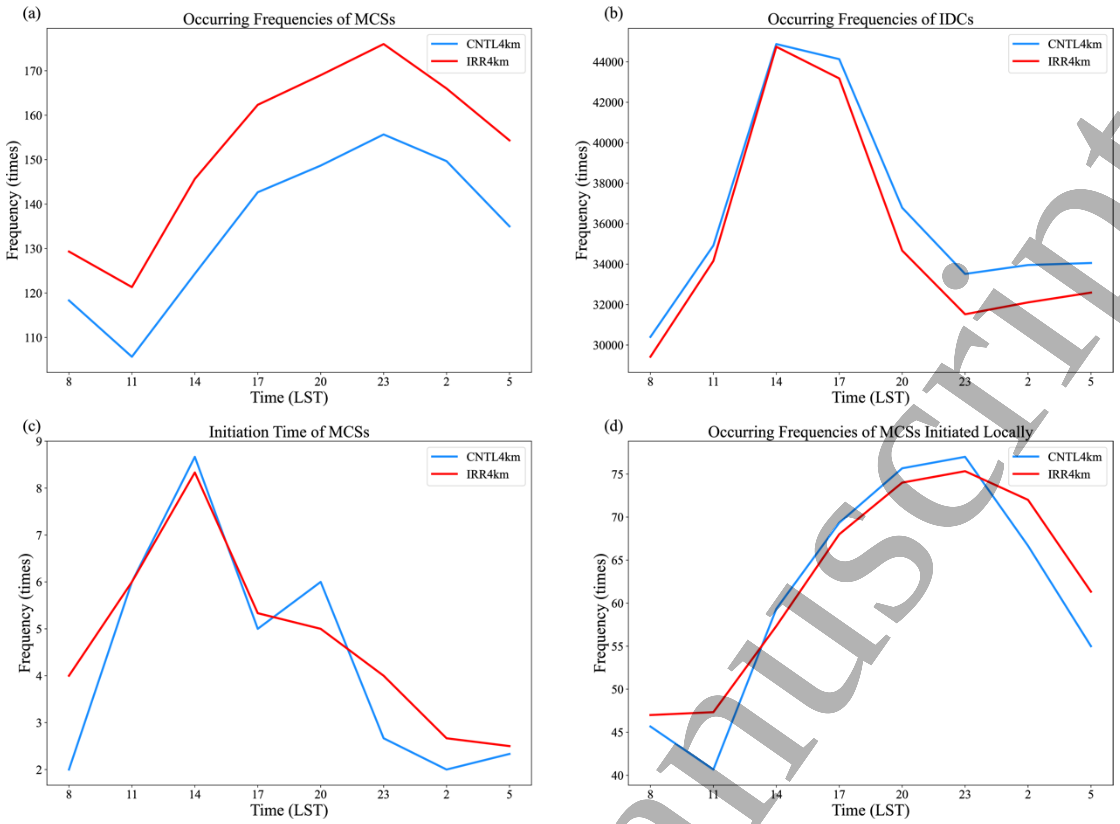

Figure 6. Diurnal cycle of (a) occurring frequencies of MCSs in the NCP, (b) IDCs in the NCP, (c) initiation time of MCSs in the NCP, and (d) MCSs locally initiated within the NCP based on the tracking run on the native 4-km model outputs.

Given the significant impacts of irrigation on regional MCS precipitation, we select MCSs which stay in the NCP for more than 3 hours (referred to as NCPMCSs) to further analyze the responses of MCSs in terms of accumulated precipitation amount, mean precipitation intensity, lifetime, spatial coverage, and propagation speed. We find that NCPMCSs, as defined by the above criterion, contribute to around 88% of the summer MCS precipitation in the NCP (figure not shown).

The probability distributions of accumulated precipitation amount and precipitation intensity of NCPMCSs are given in figure 7. The results indicate that, compared to observations (black bars in figure 7(a)), CNTL (blue bars in figure 7(a)) tends to underestimate the frequencies of weak or strong NCPMCS events in terms of accumulated precipitation amount (< 0.6 km^3 or > 8 km^3) while overestimating that with moderate precipitation amount. Similarly, CNTL underestimates the frequencies of NCPMCS events with weak or strong precipitation intensity (hourly areal precipitation) but overestimates that of moderate events (figure 7(b)). Notably, including irrigation helps mitigate the above biases (red bars in figure 7). The results based on the native 4-km model outputs are generally consistent with the 10-km re-gridded results (figure not shown).

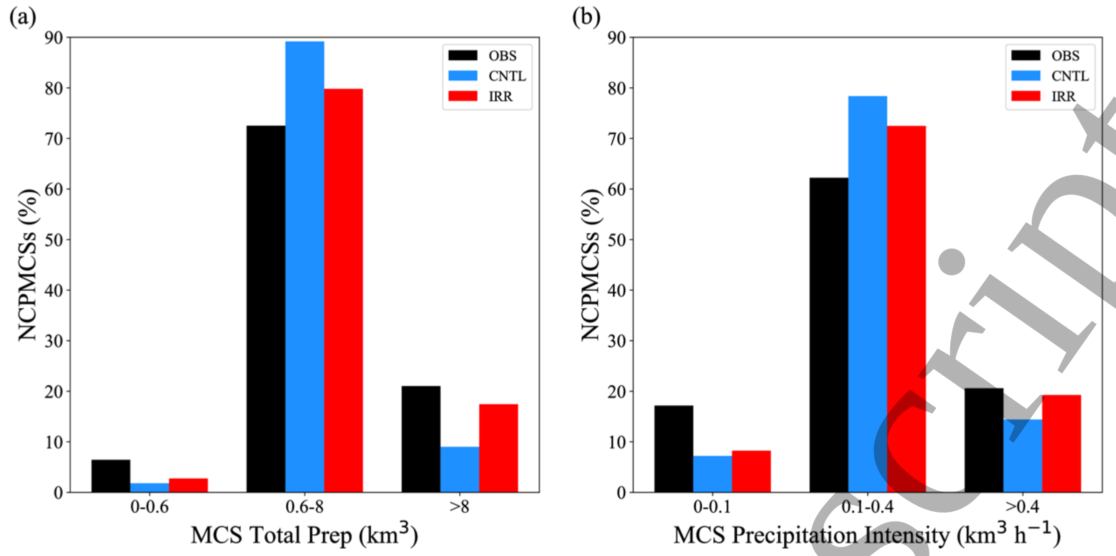

Figure 7. Probability distributions of NCPMCSs as functions of (a) accumulated precipitation amount and (b) mean precipitation intensity in observations (black), CNTL (blue), and IRR (red).

The duration and area of an MCS are crucial characteristics for quantifying its precipitation magnitude and intensity. Model results show that irrigation increases the frequency of NCPMCSs that live longer than 19 hours and cover an area larger than 120,000 km^2, aligning more closely with observations (figures 8(a) and (b)). Figure 8(c) indicates that the frequency of faster-moving MCSs is largely overestimated by CNTL, with slight improvements observed when irrigation is included.

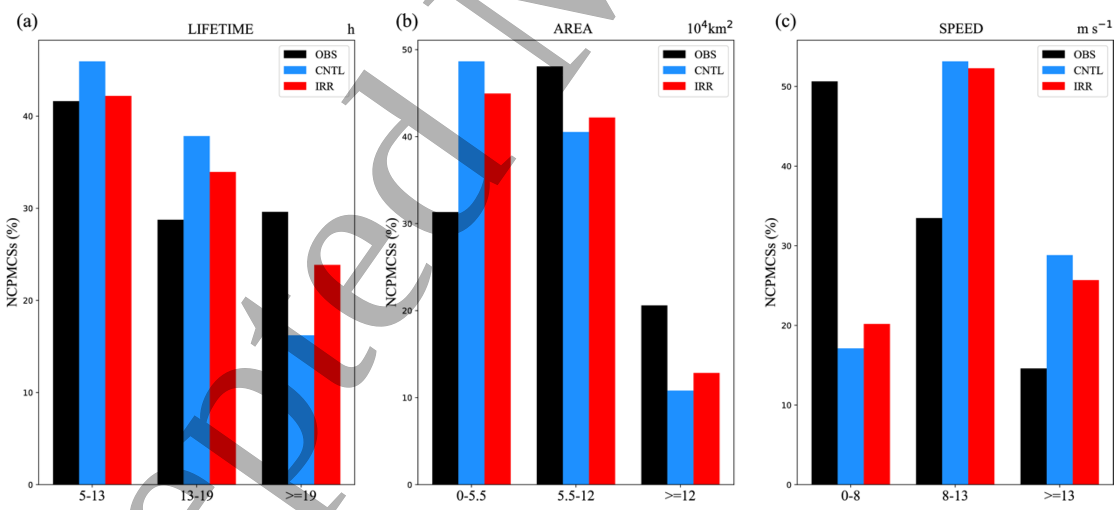

Figure 8. Probability distributions of NCPMCSs as functions of (a) lifetime, (b) average area, and (c) average propagation speed in observations (black), CNTL (blue), and IRR (red).

3.3 Response of Meteorological Conditions Associated with MCSs

As mentioned in the introduction, the impact of irrigation on precipitation involves complex land-atmosphere feedback mechanisms (Douglas *et al* 2009, Yang *et al* 2017). In figure 9 we present the vertical distributions of the irrigation-induced changes in water vapor mixing ratio, temperature, geopotential height, and vertical wind speed across the NCP (averaged for 113°–123°E). Irrigation increases lower-level water vapor due to intensified surface evaporation (Qian *et al* 2013), which is favorable for precipitation. The cooling effect of irrigation (Adegoke *et al* 2003) can extends to 700 hPa, accompanied by a baroclinic response in geopotential height which is increased at low levels but decreased at upper levels. The ascending motion is generally weakened from the surface to 500 hPa across the NCP that is dynamically unfavorable for precipitation, consistent with the findings revealed by Yang *et al* (2016). Below we focus on the irrigation-induced changes in moisture availability and atmospheric vertical motion, which respectively represent the thermodynamic and dynamical conditions for precipitation (Emori and Brown 2005, Nie *et al* 2018).

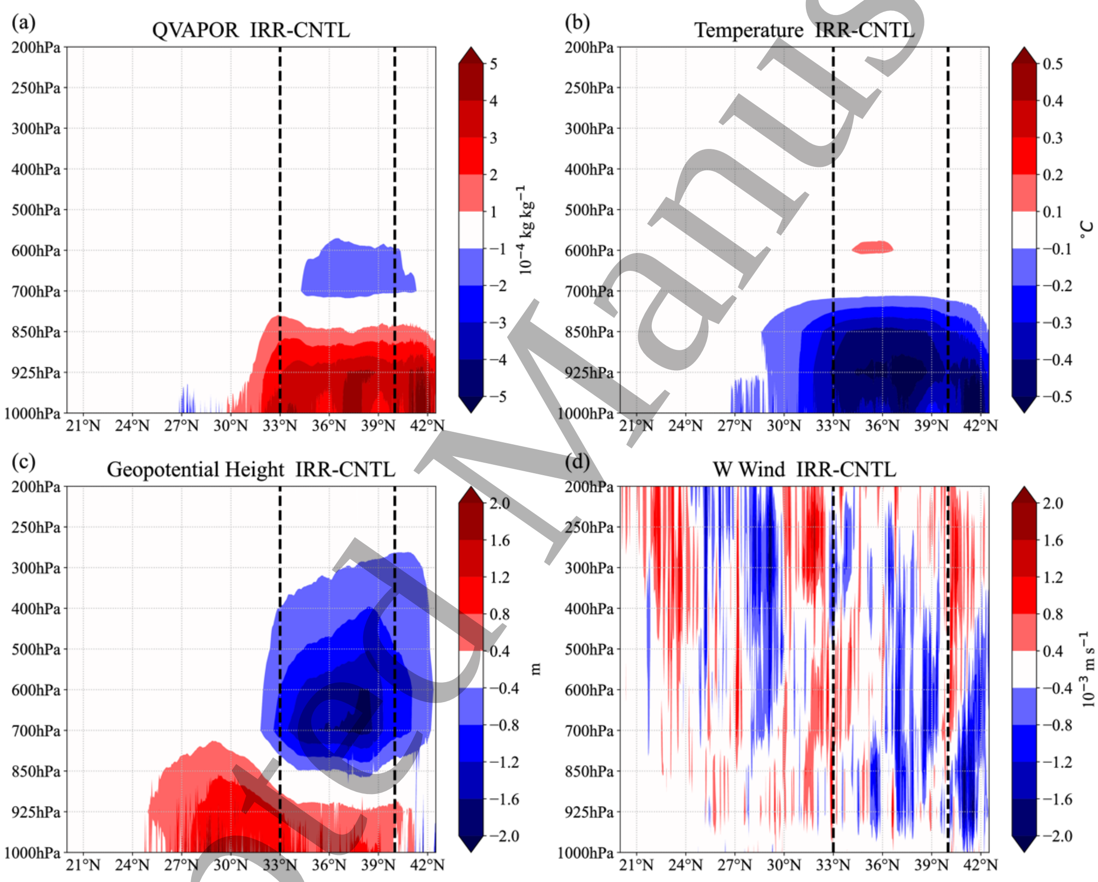

Figure 9. Pressure-latitude cross sections (averaged for 113°–123°E) of changes in (a) water vapor mixing ratio, (b) temperature, (c) geopotential height, and (d) vertical wind speed. The dashed black lines denote the latitudinal range of the NCP.

Considering that multiple MCSs might occur simultaneously in the NCP and the MCSs impacting the NCP may not always be in the NCP during their life cycle, the following analyses are based on hourly MCS precipitation averaged in the NCP rather than individual MCS events. The mean MCS precipitation, water vapor mixing ratio at 925 hPa, and vertical wind speed at 500 hPa averaged over the NCP during hours with non-negligible MCS precipitation (i.e., hourly precipitation averaged for the NCP > 10^{-5} mm) are shown in figure 10, thus denoting average large-scale conditions during MCS presence. There are a total of 1312 hours in CNTL and 1420 hours in IRR with non-negligible MCS precipitation. Consistent with the spatial distribution (figure 4(h)), the hourly MCS precipitation over the NCP is greater in IRR than in CNTL (figure 10(a)). This can be explained by the increased low-level atmospheric moisture in IRR (figures 9(a) and 10(b)), which provides a more favorable thermodynamic condition for the development of MCS. However, the thermodynamic effect is partially offset by the less favorable dynamical condition (figures 9(d) and 10(c)).

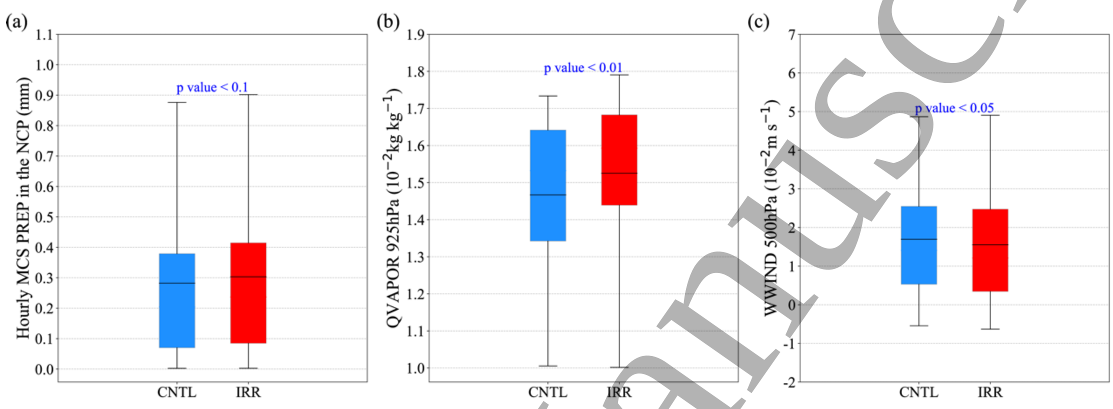

Figure 10. Boxplots of (a) hourly MCS precipitation, (b) 925 hPa water vapor mixing ratio, and (c) 500 hPa vertical wind speed averaged over the NCP during hours with non-negligible MCS precipitation (i.e., hourly precipitation averaged for the NCP > 10^{-5} mm) in CNTL (blue) and IRR (red). The mean, 25th to 75th percentile, and 5th to 95th percentile values are presented as box-and-whisker sets. The significance of differences between CNTL and IRR are denoted by p values shown in each panel beyond the boxes.

To understand the thermodynamic and dynamic conditions associated with MCSs of different precipitation intensity, we use the 50th percentile of hourly precipitation as a threshold to equally divide all the hours (with non-negligible MCS precipitation) into two (i.e., weak and strong) groups (figure 11). For the weak group, the average hourly MCS precipitation is approximately 0.1 mm and the difference between IRR and CNTL is small (figure 11(a)). The weak impact of irrigation on precipitation is mainly because the effects of the increased atmospheric moisture and weakened ascending motion largely offset each other (figures 11(b) and (c)). Compared to the weak group, the average hourly MCS precipitation in the strong group is much greater (i.e., exceeding 0.5 mm), accompanied by more sufficient atmospheric moisture and more intense ascending motion. Meanwhile, the IRR-CNTL difference in precipitation is larger than that in the weak group (figure 11(a)) because the change in ascending motion is much weaker and statistically insignificant (figure 11(c)). This is probably because the modulation effect on regional circulation of the increased condensation heating from precipitation (Nie and Fan 2019) partly offsets the surface cooling effect due to irrigation, which deserves further investigation.

It is also worth noting that in IRR, the difference in ascending motion between the weak and strong groups is larger than that in CNTL (figure 11(c)). Meanwhile, the correlation coefficient between MCS precipitation intensity and ascending motion is higher in IRR than in CNTL (i.e., 0.72 vs 0.65), while that between MCS precipitation and atmospheric moisture is lower (i.e., 0.13 vs 0.18), indicating that the variation in MCS precipitation intensity is more reflected in the variation in its dynamic condition.

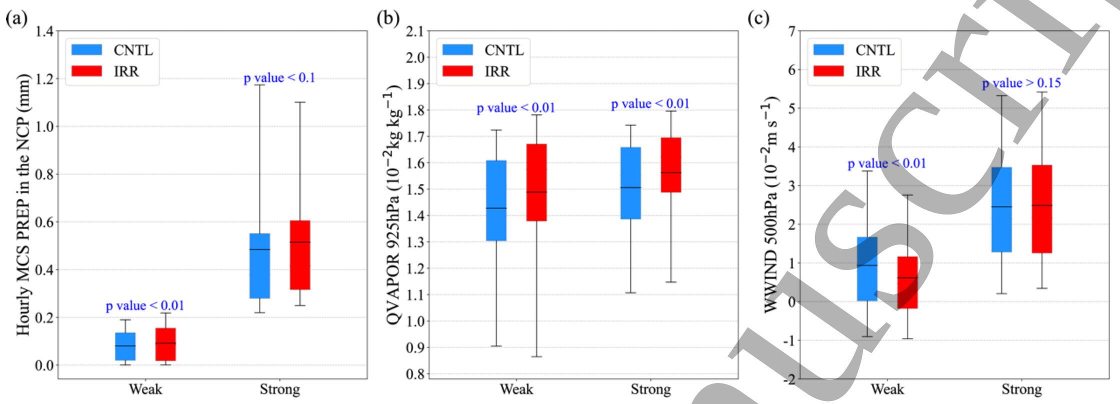

Figure 11. Boxplots of (a) hourly MCS precipitation, (b) 925 hPa water vapor mixing ratio, and (c) 500 hPa vertical wind speed averaged over the NCP during hours with weak and strong MCS precipitation in CNTL (blue) and IRR (red). The meanings of box-and-whisker sets and p values are the same as in figure 10.

4 Summary and Discussion

In this study, the WRF convection-permitting model coupled with a dynamic irrigation scheme was utilized to investigate the impacts of irrigation on summertime MCSs over the NCP. Sensitivity experiments with irrigation off and on were conducted from May 20 to August 31 over a 5-year period (2015–2019). An MCS identification and tracking algorithm was applied to both satellite observations and model simulations to quantify the response of convective systems to irrigation.

Incorporating irrigation into the WRF model significantly reduces the warm and dry biases in near-surface temperature and RH over the NCP. The inclusion of irrigation increases MCS precipitation amounts, intensity, coverage, and lifetime, aligning more closely with observations. Correspondingly, the occurring frequency of MCSs increases throughout the day, with nighttime growth attributed to more local initiation from IDCs and daytime growth mainly driven by MCSs initiating elsewhere and propagating to the NCP. The increased MCS events can be attributed to the additional moisture from intensified surface evaporation, whose effects are partially offset by the weakened atmospheric upward motion due to the cooling effect of irrigation. Compared to weak MCS precipitation events, the response of strong MCS precipitation events to irrigation is more pronounced due to the negligible offset effect of changes in large-scale ascending air motion.

Based on high-resolution numerical experiments, this study reveals the significant impacts of irrigation on MCSs over the NCP, highlighting the necessity of including irrigation in numerical models to improve precipitation simulation and prediction, especially for extreme precipitation events with strong MCSs. Nevertheless, it is imperative to acknowledge the constraints of our study, necessitating further research in the future. First, as the contribution of MCSs to precipitation can be affected by the tracking criteria used (Kukulies *et al* 2023), estimations of the irrigation effects on MCSs might be sensitive to the adjustable thresholds in the tracking algorithm. Additionally, groundwater exploitation, which is an important source of irrigation water in the NCP, can influence bottom soil moisture by altering the recharge rate and the depth of the groundwater table (Zou *et al* 2014); however, this process was not accounted for in the hydrological cycle framework of the model, potentially affecting the simulation results when the irrigation scheme is included. Furthermore, despite including the irrigation effect, significant model biases persisted, indicating considerable deficiencies in other model configurations, such as those related to land surface types, model domains, LBCs (Huang and Gao 2018, Wang and Yang 2008) and model physics (Giorgi *et al* 2002; Pieri *et al* 2015; Qian *et al* 2007). These factors can substantially impact the simulated outcomes and should be carefully considered in future studies to draw more robust conclusions. For instance, the warm biases in temperature can be related to the omission of the aerosol's cooling effects (Giorgi *et al* 2002; Qian *et al* 2007), while biases in precipitation and MCS simulations might be attributed to the uncertainties in boundary-layer processes and microphysics parameterizations (Pieri *et al* 2015). Lastly, MCSs can be affected by large-scale circulations such as the East Asian summer monsoon systems (Yang *et al* 2016), which cannot be fully reflected in regional model simulations due to the constraints from the forced lateral boundary. Global high- or variable-resolution models (Kitoh and Kusunoki 2008, Zhao *et al* 2019) should be used to better capture the response of large-scale circulations to irrigation and its impacts on MCSs.

Acknowledgments

This work is supported by the National Natural Science Foundation of China (42375049) and the Fundamental Research Funds for the Central Universities (2024300370). The contribution of Z. Y., Z. F. and Y. Q. in this study is supported by the U.S. Department of Energy's Office of Science as part of the Atmospheric System Research (ASR) program through the Integrated Cloud, Land-surface, and Aerosol System Study (ICLASS) Science Focus Area. The Pacific Northwest National Laboratory is operated for DOE by Battelle Memorial Institute under contract DE-AC05-76RL01830.

References

Adegoke J O, Pielke Sr R A, Eastman J, Mahmood R and Hubbard K G 2003 Impact of irrigation on midsummer surface fluxes and temperature under dry synoptic conditions: A regional atmospheric model study of the US High Plains *Mon. Weather Rev.* **131** 556-564

Alter R E, Fan Y, Lintner B R and Weaver C P 2015 Observational evidence that Great Plains irrigation has enhanced summer precipitation intensity and totals in the midwestern United States *J. Hydrometeorol.* **16** 1717-1735

Anabor V, Stensrud D J and de Moraes O L L 2008 Serial upstream-propagating mesoscale convective system events over southeastern South America *Mon. Weather Rev.* **136** 3087-3105

Ban N, Schmidli J and Schär C 2014 Evaluation of the convection-resolving regional climate modeling approach in decade-long simulations *J. Geophys. Res.-Atmos.* **119** 7889-7907

Crook N A 1996 Sensitivity of moist convection forced by boundary layer processes to low-level thermodynamic fields *Mon. Weather Rev.* **124** 1767-1785

DeAngelis A, Dominguez F, Fan Y, Robock A, Kustu M D and Robinson D 2010 Evidence of enhanced precipitation due to irrigation over the Great Plains of the United States *J. Geophys. Res.-Atmos.* **115**

Douglas E M, Beltrán-Przekurat A, Niyogi D, Pielke R A and Vörösmarty C J 2009 The impact of agricultural intensification and irrigation on land-atmosphere interactions and Indian monsoon precipitation - A mesoscale modeling perspective *Glob. Planet. Change* **67** 117-128

Emori S and Brown S 2005 Dynamic and thermodynamic changes in mean and extreme precipitation under changed climate *Geophys. Res. Lett.* **32**

Fan Y, Im E-S, Lan C-W and Lo M-H 2023 An increase in precipitation driven by irrigation over the North China Plain based on RegCM and WRF simulations *J. Hydrometeorol.* **24** 1155-1173

Feng Z, Hardin J, Barnes H C, Li J, Leung L R, Varble A and Zhang Z 2023a PyFLEXTRKR: A flexible feature tracking Python software for convective cloud analysis *Geosci. Model Dev.* **16** 2753-2776

Feng Z, Houze R A, Jr., Leung L R, Song F, Hardin J C, Wang J, Gustafson W I, Jr. and Homeyer C R 2019 Spatiotemporal Characteristics and Large-Scale Environments of Mesoscale Convective Systems East of the Rocky Mountains *J. Clim.* **32** 7303-7328

Feng Z, Leung L R, Hardin J, Terai C R, Song F and Caldwell P 2023b Mesoscale convective systems in DYAMOND global convection-permitting simulations *Geophys. Res. Lett.* **50** e2022GL102603

Feng Z, Leung L R, Houze Jr R A, Hagos S, Hardin J, Yang Q, Han B and Fan J 2018 Structure and evolution of mesoscale convective systems: Sensitivity to cloud microphysics in convection-permitting simulations over the United States *J. Adv. Model. Earth Syst.* **10** 1470-1494

Feng Z, Leung L R, Liu N, Wang J, Houze Jr R A, Li J, Hardin J C, Chen D and Guo J 2021 A global high-resolution mesoscale convective system database using satellite-derived cloud tops, surface precipitation, and tracking *J. Geophys. Res.-Atmos.* **126** e2020JD034202

Fosser G, Khodayar S and Berg P 2015 Benefit of convection permitting climate model simulations in the representation of convective precipitation *Clim. Dyn.* **44** 45-60

Fu S-M, Mai Z, Sun J-H, Li W-L, Ding Y and Wang Y-Q 2019 Impacts of convective activity over the Tibetan Plateau on plateau vortex, southwest vortex, and downstream precipitation *J. Atmos. Sci.* **76** 3803-3830

Giorgi F, Bi X and Qian Y 2002 Direct radiative forcing and regional climatic effects of anthropogenic aerosols over East Asia: A regional coupled climate-chemistry/aerosol model study *J. Geophys. Res.-Atmos.* **107** AAC 7-1-AAC 7-18

Gutowski W J, Jr., *et al*. 2020 The Ongoing Need for High-Resolution Regional Climate Models: Process Understanding and Stakeholder Information *Bull. Amer. Meteorol. Soc.* **101** E664-E683

Haberlie A M and Ashley W S 2019 A radar-based climatology of mesoscale convective systems in the United States *J. Clim.* **32** 1591-1606

Houze Jr R A 2004 Mesoscale convective systems *Rev. Geophys.* **42**

Houze Jr R A 2018 100 years of research on mesoscale convective systems *Meteorol. Monogr.* **59** 17.11-17.54

Hu H, Leung L R and Feng Z 2020 Understanding the distinct impacts of MCS and non-MCS rainfall on the surface water balance in the central United States using a numerical water-tagging technique *J. Hydrometeorol.* **21** 2343-2357

Hu L, Deng D, Gao S and Xu X 2016 The seasonal variation of Tibetan Convective Systems: Satellite observation *J. Geophys. Res.-Atmos.* **121** 5512-5525

Huang D and Gao S 2018 Impact of different reanalysis data on WRF dynamical downscaling over China *Atmos. Res.* **200** 25–35

Huang X, Hu C, Huang X, Chu Y, Tseng Y-h, Zhang G J and Lin Y 2018 A long-term tropical mesoscale convective systems dataset based on a novel objective automatic tracking algorithm *Clim. Dyn.* **51** 3145-3159

Huffman G, Stocker E, Bolvin D, Nelkin E and Tan J 2019 GPM IMERG final precipitation L3 half hourly 0.1 degree x 0.1 degree V06 Retrieved from Greenbelt, MD, Goddard Earth Sciences Data and Information Services Center (GES DISC) https://doi.org/10.5067/GPM/IMERG/3B-HH/06

Iacono M J, Delamere J S, Mlawer E J, Shephard M W, Clough S A and Collins W D 2008 Radiative forcing by long-lived greenhouse gases: Calculations with the AER radiative transfer models *J. Geophys. Res.-Atmos.* **113**

Janjic Z 1996 The surface layer in the NCEP Eta Model *Eleventh Conf. on Numerical Weather Prediction Norfolk, VA* 19-23

Janjic Z 2001 Nonsingular implementation of the Mellor- Yamada level 2.5 scheme in the NCEP mesoscale model. *National Centers for Environmental Prediction Office Tech. Rep.* 437

Janowiak J, Joyce B and Xie P 2017 NCEP/CPC L3 half hourly 4km global (60S -60N) merged IR V1 Retrieved from Greenbelt, MD, Goddard Earth Science s Data and Information Services Center (GES DISC) https://doi.org/10.5067/P4HZB9N27EKU

Kadaverugu R, Matli C and Biniwale R 2021 Suitability of WRF model for simulating meteorological variables in rural, semi-urban and urban environments of Central India *Meteorol. Atmos. Phys.* **133** 1379–93

Kanamitsu M and Mo K C 2003 Dynamical effect of land surface processes on summer precipitation over the southwestern United States *J. Clim.* **16** 496-509

Kang S and Eltahir E A 2018 North China Plain threatened by deadly heatwaves due to climate change and irrigation *Nat. Commun.* **9** 2894

Kang S and Eltahir E A 2019 Impact of irrigation on regional climate over Eastern China *Geophys. Res. Lett.* **46** 5499-5505

Kendon E J, Roberts N M, Senior C A and Roberts M J 2012 Realism of rainfall in a very high-resolution regional climate model *J. Clim.* **25** 5791-5806

Kitoh A and Kusunoki S 2008 East Asian summer monsoon simulation by a 20-km mesh AGCM *Clim. Dyn.* **31** 389-401

Klausmann A M 2014 Analysis of Hurricane Irene's Wind Field Using the Advanced Research Weather Research and Forecast (WRF-ARW) Model *J. Mar. Sci. Eng.* **2** 33–45

Kong F, Cai W, Shi L and Chen F 2012 The Characteristics of Annual Water Consumption for Winter Wheat and Summer Maize in North China Plain *Procedia Eng.* **28** 376–81

Kukulies J, Chen D and Curio J 2021 The role of mesoscale convective systems in precipitation in the Tibetan Plateau region *J. Geophys. Res.-Atmos.* **126** e2021JD035279

Kukulies J, Lai H-W, Curio J, Feng Z, Lin C, Li P, Ou T, Sugimoto S and Chen D 2023 Mesoscale convective systems in the third pole region: Characteristics, mechanisms and impact on precipitation *Front. Earth Sci.* **11**

Laing A G and Michael Fritsch J 1997 The global population of mesoscale convective complexes *Q. J. R. Meteorol. Soc.* **123** 389-405

Li J, Qian Y, Leung L R, Feng Z, Sarangi C, Liu Y and Yang Z 2022 Impacts of large-scale urbanization and irrigation on summer precipitation in the mid-Atlantic region of the United States *Geophys. Res. Lett.* **49** e2022GL097845

Li P, Moseley C, Prein A F, Chen H, Li J, Furtado K and Zhou T 2020 Mesoscale convective system precipitation characteristics over East Asia. Part I: Regional differences and seasonal variations *J. Clim.* **33** 9271-9286

Liang S, *et al.* 2021 The global land surface satellite (GLASS) product suite *Bull. Amer. Meteorol. Soc.* **102** E323-E337

Liu J, Jin J and Niu G Y 2021 Effects of irrigation on seasonal and annual temperature and precipitation over China simulated by the WRF model *J. Geophys. Res.-Atmos.* **126** e2020JD034222

Lucas-Picher P, Argüeso D, Brisson E, Tramblay Y, Berg P, Lemonsu A, Kotlarski S and Caillaud C 2021 Convection-permitting modeling with regional climate models: Latest developments and next steps *Wiley Interdiscip. Rev.-Clim. Chang.* **12** e731

Mahmood R, Foster S A, Keeling T, Hubbard K G, Carlson C and Leeper R 2006 Impacts of irrigation on 20th century temperature in the northern Great Plains *Glob. Planet. Change* **54** 1-18

Markowski P and Richardson Y 2010 Mesoscale Convective Systems *John Wiley & Sons, Ltd* **10.1002/9780470682104** 245-272

Mo X-G, Hu S, Lin Z-H, Liu S-X and Xia J 2017 Impacts of climate change on agricultural water resources and adaptation on the North China Plain *Adv. Clim. Chang. Res.* **8** 93–8

Nakanishi M and Niino H 2006 An improved Mellor–Yamada level-3 model: Its numerical stability and application to a regional prediction of advection fog *Bound.-Layer Meteor.* **119** 397-407

Nesbitt S W, Cifelli R and Rutledge S A 2006 Storm morphology and rainfall characteristics of TRMM precipitation features *Mon. Weather Rev.* **134** 2702-2721

Nie J and Fan B 2019 Roles of dynamic forcings and diabatic heating in summer extreme precipitation in East China and the southeastern United States *J. Clim.* **32** 5815-5831

Nie J, Sobel A H, Shaevitz D A and Wang S 2018 Dynamic amplification of extreme precipitation sensitivity *Proc. Natl. Acad. Sci.* **115** 9467-9472

Ozdogan M, Rodell M, Beaudoing H K and Toll D L 2010 Simulating the effects of irrigation over the United States in a land surface model based on satellite-derived agricultural data *J. Hydrometeorol.* **11** 171-184

Pei L, Moore N, Zhong S, Kendall A D, Gao Z and Hyndman D W 2016 Effects of irrigation on summer precipitation over the United States *J. Clim.* **29** 3541-3558

Pielke Sr R A 2001 Influence of the spatial distribution of vegetation and soils on the prediction of cumulus convective rainfall *Rev. Geophys.* **39** 151-177

Pieri A B, Hardenberg J von, Parodi A and Provenzale A 2015 Sensitivity of Precipitation Statistics to Resolution, Microphysics, and Convective Parameterization: A Case Study with the High-Resolution WRF Climate Model over Europe *J. Hydrometeorol.* **16** 1857–72

Prein A F, Liu C, Ikeda K, Bullock R, Rasmussen R M, Holland G J and Clark M 2020 Simulating North American mesoscale convective systems with a convection-permitting climate model *Clim. Dyn.* **55** 95-110

Qian Y, Huang M, Yang B and Berg L K 2013 A modeling study of irrigation effects on surface fluxes and land–air–cloud interactions in the Southern Great Plains *J. Hydrometeorol.* **14** 700-721

Qian Y, Wang W, Leung L R and Kaiser D P 2007 Variability of solar radiation under cloud-free skies in China: The role of aerosols *Geophys. Res. Lett.* **34**

Qian Y, Yang Z, Feng Z, Liu Y, Gustafson W I, Berg L K, Huang M, Yang B and Ma H-Y 2020 Neglecting irrigation contributes to the simulated summertime warm-and-dry bias in the central United States *npj Clim. Atmos. Sci.* **3** 31

Rasmussen K L, Chaplin M M, Zuluaga M D and Houze R A 2016 Contribution of Extreme Convective Storms to Rainfall in South America *J. Hydrometeorol.* **17** 353-367

Sacks W J, Cook B I, Buenning N, Levis S and Helkowski J H 2009 Effects of global irrigation on the near-surface climate *Clim. Dyn.* **33** 159-175

Salio P, Nicolini M and Zipser E J 2007 Mesoscale convective systems over southeastern South America and their relationship with the South American low-level jet *Mon. Weather Rev.* **135** 1290-1309

Schumacher R S and Rasmussen K L 2020 The formation, character and changing nature of mesoscale convective systems *Nat. Rev. Earth Environ.* **1** 300-314

Siebert S, Burke J, Faures J-M, Frenken K, Hoogeveen J, Döll P and Portmann F T 2010 Groundwater use for irrigation–a global inventory *Hydrol. Earth Syst. Sci.* **14** 1863-1880

Siebert S, Henrich V, Frenken K and Burke J 2013 *Update of the digital global map of irrigation areas to version 5.*

Skamarock W C, *et al*. 2019 A description of the advanced research WRF version 4 *NCAR tech. note ncar/tn-556+ str* **145**

Smith B T, Thompson R L, Grams J S, Broyles C and Brooks H E 2012 Convective modes for significant severe thunderstorms in the contiguous United States. Part I: Storm classification and climatology *Weather Forecast.* **27** 1114-1135

Starzec M, Homeyer C R and Mullendore G L 2017 Storm Labeling in Three Dimensions (SL3D): A Volumetric Radar Echo and Dual-Polarization Updraft Classification Algorithm Mon. *Weather Rev.* **145** 1127-1145

Stevenson S N and Schumacher R S 2014 A 10-year survey of extreme rainfall events in the central and eastern United States using gridded multisensor precipitation analyses *Mon. Weather Rev.* **142** 3147-3162

Tewari M 2004 Implementation and verification of the unified NOAH land surface model in the WRF model *20th Conf. on Weather Analysis and Forecasting/16th Conf. on Numerical Weather Prediction* 11-15

Thompson G, Field P R, Rasmussen R M and Hall W D 2008 Explicit forecasts of winter precipitation using an improved bulk microphysics scheme. Part II: Implementation of a new snow parameterization *Mon. Weather Rev.* **136** 5095-5115

Tiedtke M 1989 A comprehensive mass flux scheme for cumulus parameterization in large-scale models *Mon. Weather Rev.* **117** 1779-1800

Wang B and Yang H 2008 Hydrological issues in lateral boundary conditions for regional climate modeling: simulation of east asian summer monsoon in 1998 *Clim. Dyn.* **31** 477–90

Wu D, Fang S, Li X, He D, Zhu Y, Yang Z, Xu J and Wu Y 2019 Spatial-temporal variation in irrigation water requirement for the winter wheat-summer maize rotation system since the 1980s on the North China Plain *Agric. Water Manage.* **214** 78–86

Wu J and Gao X-J 2013 A gridded daily observation dataset over China region and comparison with the other datasets *Chinese J. Geophys.-Chinese Ed.* **56** 1102-1111

Wu J, Gao X, Giorgi F and Chen D 2017 Changes of effective temperature and cold/hot days in late decades over China based on a high resolution gridded observation dataset *Int. J. Climatol.* **37** 788-800

Yang B, Zhang Y, Qian Y, Tang J and Liu D 2016 Climatic effects of irrigation over the

Huang-Huai-Hai Plain in China simulated by the weather research and forecasting model *J. Geophys. Res.-Atmos.* **121** 2246-2264

Yang R, Zhang Y, Sun J, Fu S and Li J 2019 The characteristics and classification of eastward-propagating mesoscale convective systems generated over the second-step terrain in the Yangtze River Valley *Atmos. Sci. Lett.* **20** e874

Yang X, Fei J, Huang X, Cheng X, Carvalho L M and He H 2015 Characteristics of mesoscale convective systems over China and its vicinity using geostationary satellite FY2 *J. Clim.* **28** 4890-4907

Yang Z, Dominguez F, Zeng X, Hu H, Gupta H and Yang B 2017 Impact of irrigation over the California Central Valley on regional climate *J. Hydrometeorol.* **18** 1341-1357

Yang Z, Varble A, Berg L K, Qian Y, Tai S L, Chen J, Gustafson Jr W I, Feng Z and Liu Y 2023 Sensitivity of Precipitation Displacement of a Simulated MCS to Changes in Land Surface Conditions *J. Geophys. Res.-Atmos.* **128** e2022JD037642

Yuan J and Houze R A 2010 Global variability of mesoscale convective system anvil structure from A-Train satellite data *J. Clim.* **23** 5864-5888

Yun Y, Liu C, Luo Y and Gao W 2021 Warm-season mesoscale convective systems over eastern China: convection-permitting climate model simulation and observation *Clim. Dyn.* **57** 3599-3617

Zhang C, Wang Y and Hamilton K 2011 Improved representation of boundary layer clouds over the southeast Pacific in ARW-WRF using a modified Tiedtke cumulus parameterization scheme *Mon. Weather Rev.* **139** 3489-3513

Zhang H-L, Zhao X, Yin X-G, Liu S-L, Xue J-F, Wang M, Pu C, Lal R and Chen F 2015 Challenges and adaptations of farming to climate change in the North China Plain *Clim. Change* **129** 213-224

Zhang L, Min J, Zhuang X and Schumacher R S 2019 General features of extreme rainfall events produced by MCSs over East China during 2016–17 *Mon. Weather Rev.* **147** 2693-2714

Zhang Y, Zhang F, Davis C A and Sun J 2018 Diurnal evolution and structure of long-lived mesoscale convective vortices along the mei-yu front over the East China plains *J. Atmos. Sci.* **75** 1005-1025

Zhao C, Xu M, Wang Y, Zhang M, Guo J, Hu Z, Leung L R, Duda M and Skamarock W 2019 Modeling extreme precipitation over East China with a global variable-resolution modeling framework (MPASv5.2): impacts of resolution and physics *Geosci. Model Dev.* **12** 2707-2726

Zou J, Xie Z, Yu Y, Zhan C and Sun Q 2014 Climatic responses to anthropogenic groundwater exploitation: a case study of the Haihe River Basin, Northern China *Clim. Dyn.* **42** 2125-2145